Project Title: Dislocation - Radiation Obstacle Interactions: Developing Improved Mechanical Property Constitutive Models

Date of Report: 10 October 2008

Recipient: University of Illinois, Department of Materials Science and Engineering.

Award Number: DE-FC07-04ID14595

Subcontractors: None

Other Partners: Brian Wirth, University of California- Berkeley.

Contact(s): Ian M. Robertson, 217 333 1440, ianr@uiuc.edu

Project Team: DOE Project Manager: Nancy Elizondo; Contract Specialist: Seb Klein; Contracting Officer: T. Wade Hillebrant

Project Objective: The objective of this program was to understand the interaction of dislocations with a wide range of obstacles commonly produced in materials under irradiation (dislocation loops, voids, helium bubbles, stacking fault tetrahedra and radiation-induced precipitates). The approach employed in this program combined multi-scale modeling and dynamic in-situ and static ex-situ transmission electron microscopy experiments. This report is concerned with the experimental aspects of the program.

Background: The materials for use in Generation IV and Advanced Fuel Cycle Initiatives present significant material challenges and opportunities [1]. The materials will be required to function at higher temperatures and in more aggressive environments than current reactor-grade materials. These changes in operational conditions place stringent demands on material properties. Creep, fatigue, and creep-fatigue interactions will become important damage mechanisms along with irradiation effects and corrosion. Neutron radiation damage to structural and cladding materials in current nuclear environments (Generation I and II reactor systems) produces significant mechanical property degradation [2-10]. However, despite extensive effort which has produced a significant body of knowledge regarding the macroscopic degradation in properties, our insight to the fundamental processes is only beginning to be revealed and current models remain predominantly empirical. A consequence of this lack of predictive capability is that rapid assessment on the applicability of new candidate alloy systems is hindered.

The development of predictive models requires input of the essential features of the dominant deformation processes over multiple length and time scales. The work conducted in this program utilized the latest advances in computational science and analytical experimental techniques to develop a fundamental understanding of dislocation interactions with the obstacles commonly observed in irradiated materials (e.g., dislocation loops, voids, helium bubbles, and stacking-fault tetrahedra). The program is divided into an experimental and a computational component with the latter being conducted at the University of California at Berkeley under the direction of Professor Brian Wirth; this component is reported on separately. Ultimately, the insight regarding dislocation-obstacle behavior gleaned from this study will be incorporated in higher length-scale models to predict the post-yield constitutive properties of irradiated materials.

Figure 1 provides a schematic illustration of a multi-scale approach to modeling the plastic response of metals [11]. The ultimate goal is to model the behavior at different length and time scales within one grand multi-scale scheme. Within this approach, first principal simulations yield the interatomic interactions; molecular dynamics computer simulations determine interatomic processes on the Ångstrom length scale; and dislocation dynamics the long-range interactions on the micrometer length scale. This then provides the basis on which to develop continuum models of deformation and fracture mechanics which are used to predict material responses. The overlapping circles are indicative of junctions in length and time scales between the different methods. Also, shown in the figure are experimental approaches that can provide information at appropriate length and time scales. This integrated approach is seen as key to the development of physically-based predictive models of material properties. In this program our approach is to use electron microscopy, especially time-resolved experimental techniques *in situ* in the electron microscope, along with molecular dynamics computer simulation to reveal the atomistic processes responsible for controlling the interaction between dislocations and irradiation produced defects.

To illustrate how this combined approach can lead to a predictive model, we considered how defect-free channels are created by the sweeping action of dislocations and how this action results in a loss of ductility, an increase in the yield and tensile strength, and the appearance of the apparent yield point in irradiated FCC materials. The *in situ* TEM studies showed that the dislocations responsible for creating the defect-free channels originated from grain boundaries and stress concentrators and not from pre-existing dislocations, defects were not necessarily

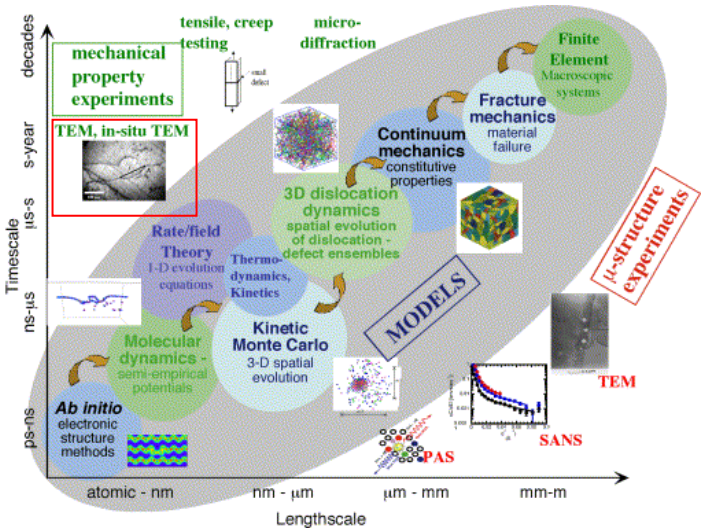

Figure. 1. Illustration of an integrated experimental and computational approach to the multi-scale investigation of materials behavior in the fusion environment. The central part of the figure describes a hierarchical approach based on passing information or parameters, and connecting key mechanisms (denoted by arrows), starting from the electronic/atomic up to structural length and time scales. A number of microstructural characterization techniques important for validating model predictions are represented on the lower right side, including the techniques of positron annihilation spectroscopy (PAS), small angle neutron scattering (SANS) and transmission electron microscopy (TEM). The upper left side of the diagram represents experimental techniques to measure mechanical properties [11].

annihilated by the interaction with just one dislocation, and that the obstacle strength for any defect is not constant but is variable and depends on the size and type of the defect, location of the intersection of the glide plane on the defect, and that the nature of the dislocation, and the interaction may change the defect from one type to another [12, 13]. A crystal plasticity model based on the dispersed-barrier hardening concept was developed that included the effect of decreasing the effective hardness of radiation defects as the mobile dislocations shear them and that the preexisting dislocations do not contribute significantly to the total plasticity [14]. Another critical concept was making the resistance to dislocation glide proportional to the sum of the obstacle densities rather than the sum of individual resistance contributions. Figure 2 shows the stress-strain curves generated as a function of defect density (neutron exposure). The results show striking similarities with experimental observations [4, 10, 15-19]. Despite the success of the model it is important to appreciate that several effects are still included phenomenologically. For example, the variation in obstacle strength was incorporated through the obstacle size. This captures the effect, but fails to account for the geometric component related to the location on the obstacles that the slip plane impacts. It also does not capture the effect of the defect population evolving from one type to another or decreasing in size during the course of the deformation process – both processes will change the obstacle strength.

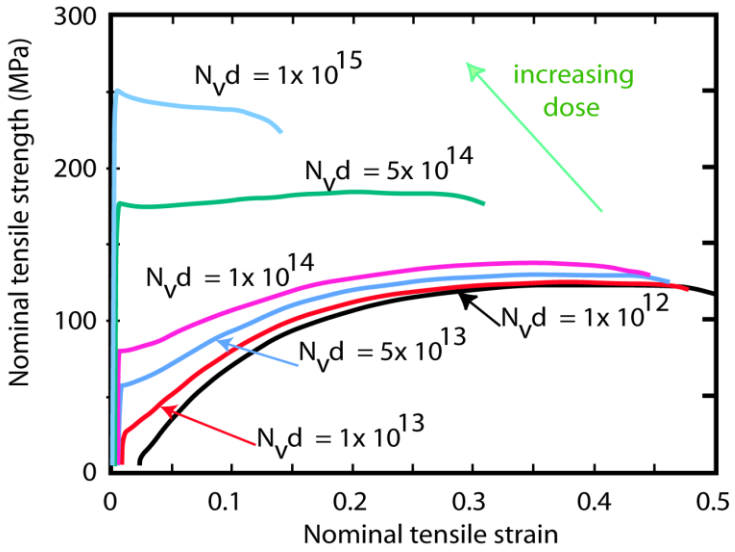

Figure 2. Predictions of the stress-strain relation as a function of increasing dose[13,14].

The emphasis of this project was on the interaction of dislocations with obstacles commonly produced in irradiated materials such as stacking-fault tetrahedra, helium bubbles, and dislocation loops. The specimens were deformed in a discontinuous manner *in-situ* in either a Philips CM12 TEM operating at 120 keV or a JEOL 2010 TEM operating at 200 keV. Defect interactions were observed and recorded with an analog TV camera as well as a CCD system with capture rates of 30 frames per second and 20 images per second, respectively. In the latter case, four times binning allows for a capture rate of 20 images per second at a resolution of 720 x 480. Higher capture rates are attainable but with a concomitant sacrifice in image resolution. These images are post-processed using an image processing system, which allows an image-by-image analysis to be performed.

In-situ elevated temperature straining experiments were performed at a nominal temperatures > 500 K in a single-tilt heating holder (Gatan Model 672). This stage has a theoretical use temperature of about 1000K, but the stage design is such that the sample is not in

intimate contact with the heating element. Consequently, there is a large disparity between the heater and the sample temperature. Ex-situ calibration of this stage shows a difference between the sample and heater temperature to be as much as 150 degrees, although during a test this difference can be rapidly negated if the sample comes in intimate contact with the heating element. This places a limit of what can be achieved with this stage unless the sample has some intrinsic calibration mechanism – loss of a precipitate phase at a particular temperature, for example. Nevertheless this stage can be used to observe and understand unit processes occurring during elevated temperature deformation [20].

In the following, the key observations from each of these interactions are highlighted.

Dislocation Interactions with Stacking-fault Tetrahedra.

In low stacking-fault energy FCC metals, stacking-fault tetrahedra are common defects that can be produced by different treatments, such as irradiation [21-23], ageing after quenching from temperatures close to the melting temperature [22, 24-26], and heavy plastic deformation[27, 28]. The approach used in this study was to age quenched Au to control the size, distribution and density of stacking-fault tetrahedra. Specifically, samples of Au for *in situ* TEM straining with dimensions 11.5mm x 2.5 mm were cut from 99.999% pure gold sheet that was 200 μm-thick, annealed at 1273K for 1 hour, quenched in iced brine and then aged for example for one hour at 373K. In-situ TEM straining specimens were electropolished to perforation using a twin-jet apparatus with an electrolyte solution consisting of KCN 67 g per liter water at 273 K using a current density of 0.12 A cm^{-2}.

An example of the initial field of stacking-fault tetrahedra produced in quenched and aged gold is shown in the bright-field image presented in Figure 3; in this orientation the tetrahedra appear as triangular defects. Both fully formed and truncated tetrahedra were observed. The average size of tetrahedra was 51.18 ± 11.43 nm, as determined from measurement of the side length of the tetrahedron; it is important to note that it has not been verified if this length corresponds to the actual dimensions of the defect. Three different interactions between a moving dislocation and stacking-fault tetrahedron were observed during in-situ straining at nominal temperatures > 500 K, including shearing of the tetrahedron followed by complete restoration, absorption of the stacking-fault tetrahedron on the dislocation and its subsequent annihilation, and conversion of a tetrahedron to another defect type. In the following, examples of the different interactions are shown.

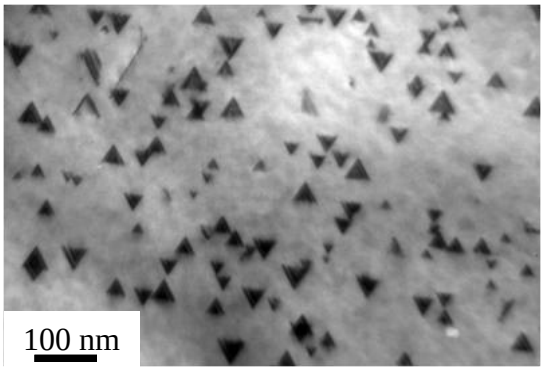

Figure 3. Bright-field electron micrograph showing a field of stacking fault tetrahedra produced by ageing the quenched-in vacancy population.

The initial position of the dislocation and the tetrahedra are shown in the bright-field image presented in Figure 4a. In this image, it can be seen that at one end of the dislocation the line direction changes abruptly several times. The first change in direction corresponds to the dislocation having cross-slipped, the second to it returning to the original slip system, and the third to it having cross-slipped again. For the purpose of describing the interactions, the

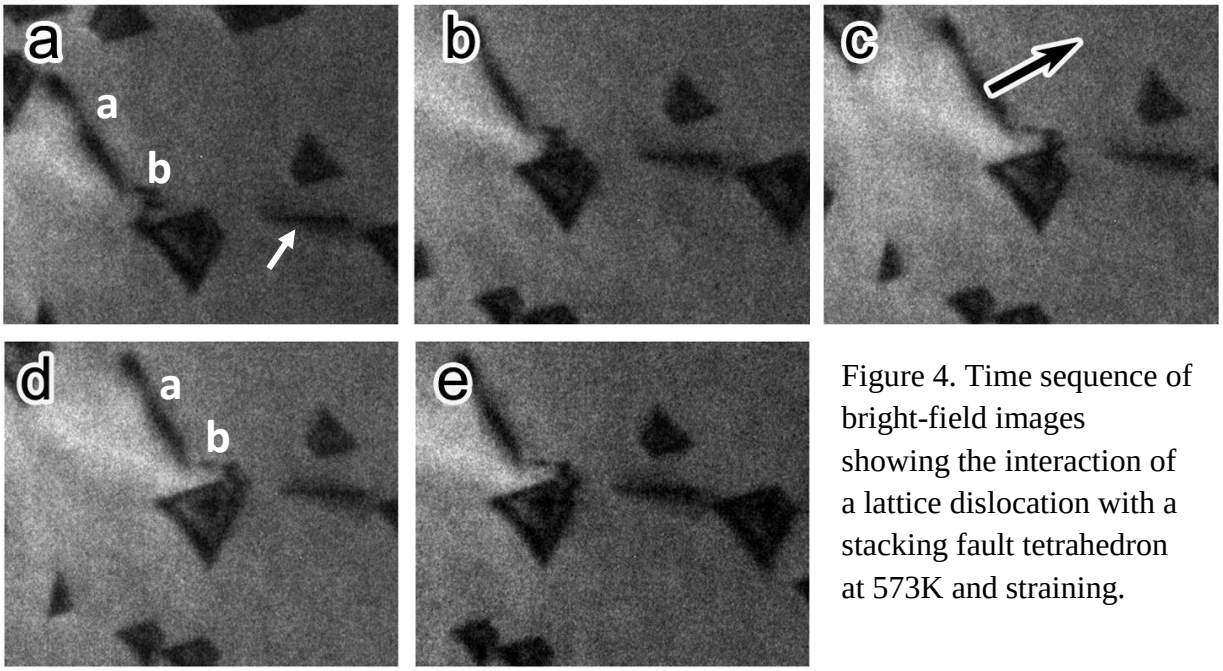

Figure 4. Time sequence of bright-field images showing the interaction of a lattice dislocation with a stacking fault tetrahedron at 573K and straining.

dislocation component on the primary slip plane is designated "*a*" and that on the cross-slip plane "*b"*. The interaction with the first tetrahedron involves the end dislocation segment on the cross-slip plane. This interaction appears to leave the tetrahedron unchanged; the only indication of a reaction evident in the still images presented is the extension of the cross-slipped component of the dislocation; compare the line lengths of the various segments in Figures 4b and 4 c-e. In practice, and evident in the video, is that the progress of the dislocation is retarded by the interaction.

Although the Burgers vector and line direction of the dislocation were not determined specifically in this case, it is possible to infer them from the nature of the interactions in which the dislocation is involved. With the foil normal coming out of the plane of the paper, the configuration of the tetrahedron in the matrix is shown in the schematic presented in Figure 5; the tetrahedron is indexed using Thompson's notation [29]. From consideration of all the interactions in which this dislocation was involved, it can be surmised that it is of mixed character and is mobile on the *c-plane (ABD)* initially; it is appreciated that it is only the screw

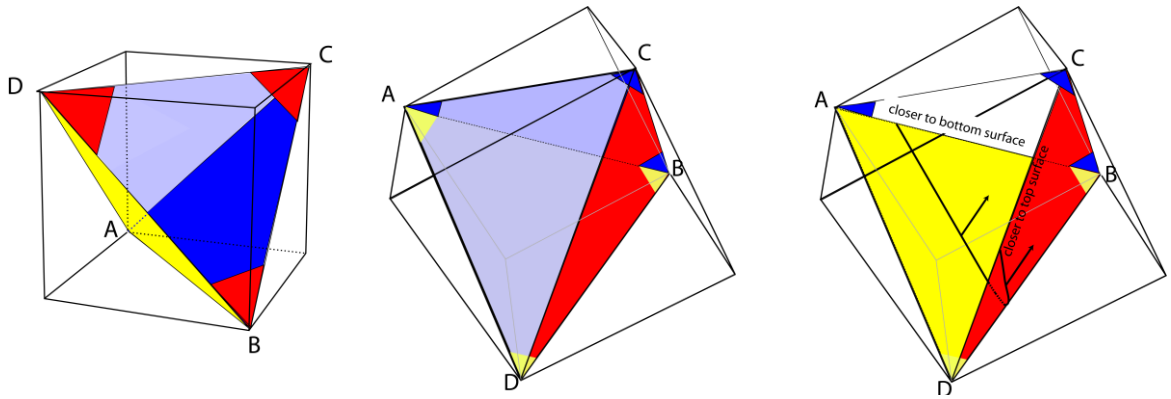

Figure 5. a) Tetrahedron with planes indicated. (BCD) front plane shown in red. b) approximate configuration for interaction shown in Figure 4. c) dislocation on slip planes.

segment that is capable of cross-slip. Early in the interaction sequence a portion of the dislocation cross slips to the *a-plane (DBC)* indicating it has a Burgers vector DB; the dislocation orientation is shown in Figure 5c along with the primary and cross-slip planes.

After the first interaction, the same dislocation, although now with a distinct "v-shape," breaks away from this tetrahedron and moves rapidly towards the truncated tetrahedron, arrowed in Figures 4a and 6a. The time between the first two frames in Figure 6 is $34/100^{th}$ of a second (one frame) and the resulting annihilation of the tetrahedron is significant as evidenced by the change in line length: the white line in Figure 6b corresponds to the original side length of the tetrahedron and it is clearly longer than that of the remaining component. The annihilation of the remainder of the tetrahedron takes longer and results in the component of the dislocation on the *a-plane* moving in front of the component on the *c-plane*, see Figure 6c.

Partial annihilation of a stacking-fault tetrahedron can be achieved by the interaction with

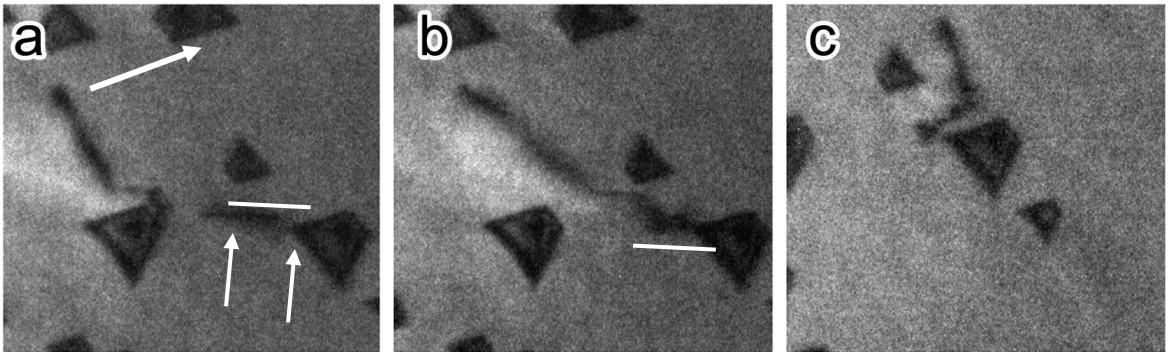

Figure 6. Annihilation of a truncated stacking-fault tetrahedron by a dislocation at 573 K.

a line dislocation. An example of this type of interaction is shown in the series of images presented in Figure 7. This is the same dislocation as in Figures 4 and 6. The component of the dislocation on the *a-plane* remains trapped in an interaction with another tetrahedron while the component on the *c-plane* moves forward. This interaction is similar to that described in Figure 4. Here it is clear that motion of the segment on the cross-slip plane is retarded by the interaction with the tetrahedron. As the *a-plane* dislocation component breaks free from the tetrahedron it moves rapidly ahead of the other component towards the next tetrahedron. The dislocation again has a complex line direction and has cross-slipped several times; the segments on the different slip planes are labeled. The end segment *b* interacts with the tetrahedron, Figures 7d and 7e. The consequence of this interaction, see Figures 7f through 7i, is annihilation of the tetrahedron and the generation of a defect with projected line directions approximately parallel to AD and DC. Some collapse of this defect occurs with time as can be seen by comparing Figures 7h and 7i. Dislocation segment *a* breaks free as this tetrahedron collapses and moves to interact with the next tetrahedron, Figure 7i. The entire interaction is rapid lasting for just over one second; the collapse occurs within two image captures, approximately 0.1 seconds.

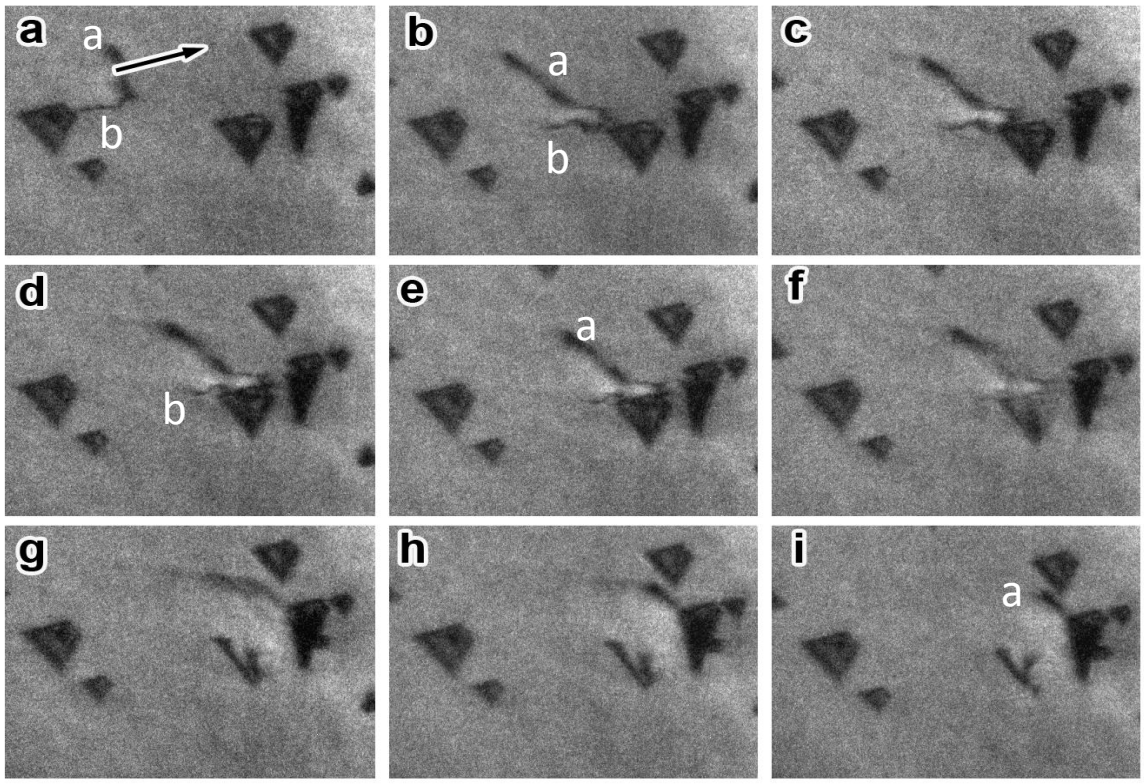

Figure 7. Conversion of a stacking-fault tetrahedron to a new defect.

A possible explanation for the interaction is shown in the series of schematics presented in Figure 8. The dipole segment on the *a-plane* impacts the tetrahedron on the *c-plane*, where it dissociates to partial dislocations on the *c-plane* according to the reaction $DB \rightarrow D\gamma+\gamma B$. The partial dislocations move on the *c-plane,* unfaulting this plane as they move. They interact with the bounding stair-rod dislocations to produce partial dislocations that are glissile on the other {111} planes. For example, the partial dislocation $D\gamma$ interacts with the stair-rod dislocations $\gamma\beta$ to produce $D\beta$, which is glissile on the *b-plane*, and with $\gamma\delta$ to produce $D\delta$, which is mobile on the *d-plane*. The other partial dislocation interacts with $\gamma\beta$ to produce γB, and with $\gamma\alpha$ to produce αB, which are glissile on the *b-* and *a-planes*, respectively. These interactions are shown in Figure 8b. This process continues on the other faces of the tetrahedron as shown schematically in Figures 8c and 8d. The end result is the elimination of the stacking-fault tetrahedron and the formation of a helical twist on the dislocation. In this case the non-interacting dislocation segment continues to move forward, pinching off the dislocation segment interacting with the tetrahedron, as illustrated schematically in Figure 8c. This pinching off most likely coincides with the expanding segment contacting the foil surface, which will break up the expanding loop. The dislocation line associated with the tetrahedron collapses to the configuration shown in Figure 8i, which is equivalent to the helical segment of the classic unfaulting interaction proposed by Kimura and Maddin.[30] This dislocation can obviously act as an obstacle to motion of other dislocations and would have a different obstacle strength than a stacking-fault tetrahedron.

To determine if higher temperatures were needed to influence the interactions further experiments were performed at a nominal temperature of 616 K. An interaction of a dislocation

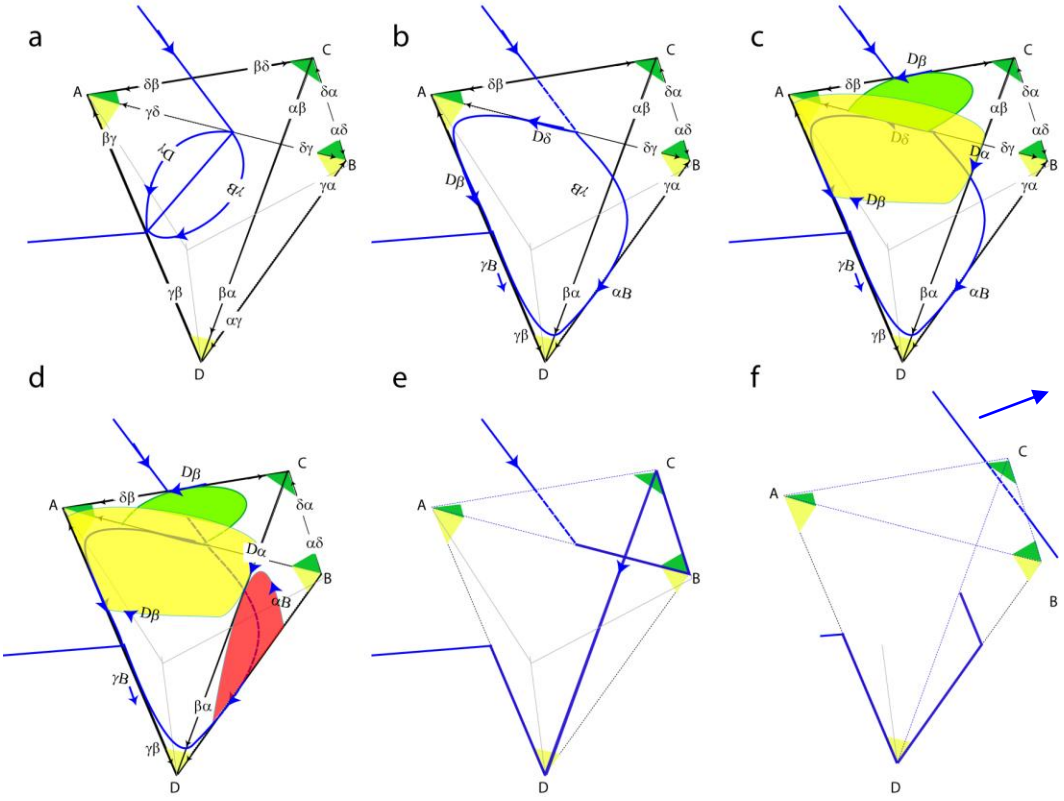

Figure 8. Schematic showing a possible unfaulting reaction that leads to the dislocation configuration shown in Figure 7.

with an isolated tetrahedron at 616 K is shown in the series of images presented in Figure 9. The initial position of the dislocation with respect to the tetrahedron is shown in Figure 9a; the direction of dislocation motion is indicated by the arrow and the arrowhead marks a common feature in all images. The dislocation approaches the stacking-fault tetrahedron, Figure 9b, interacts with and annihilates it leaving no remnant defect, Figure 9c. It was noticed that the dislocation cross-slipped prior to the interaction with the tetrahedron. The orientation of the stacking-fault tetrahedron was deduced by placing the directions ascertained from the diffraction pattern back on to the image; the tetrahedron is indexed using Thompson's notation. The dislocation has a screw character and its Burgers vector was determined to be (110) CD.

The series of video-frame images shown in Figure 10 presents the interaction between a moving dislocation and 3 different stacking fault tetrahedra at 616 K. Here two stacking-fault tetrahedra were total annihilated and one was partially annihilated leaving behind a small

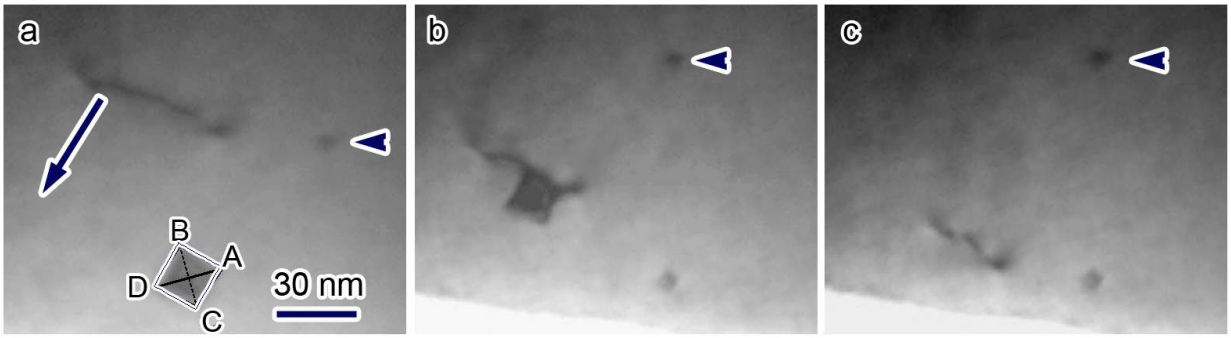

Figure 9. Bright-field electron micrographs of the interaction between a perfect stacking-fault tetrahedron and dislocation at 616 K. As result of the interaction the tetrahedron was annihilated and no remnant produced.

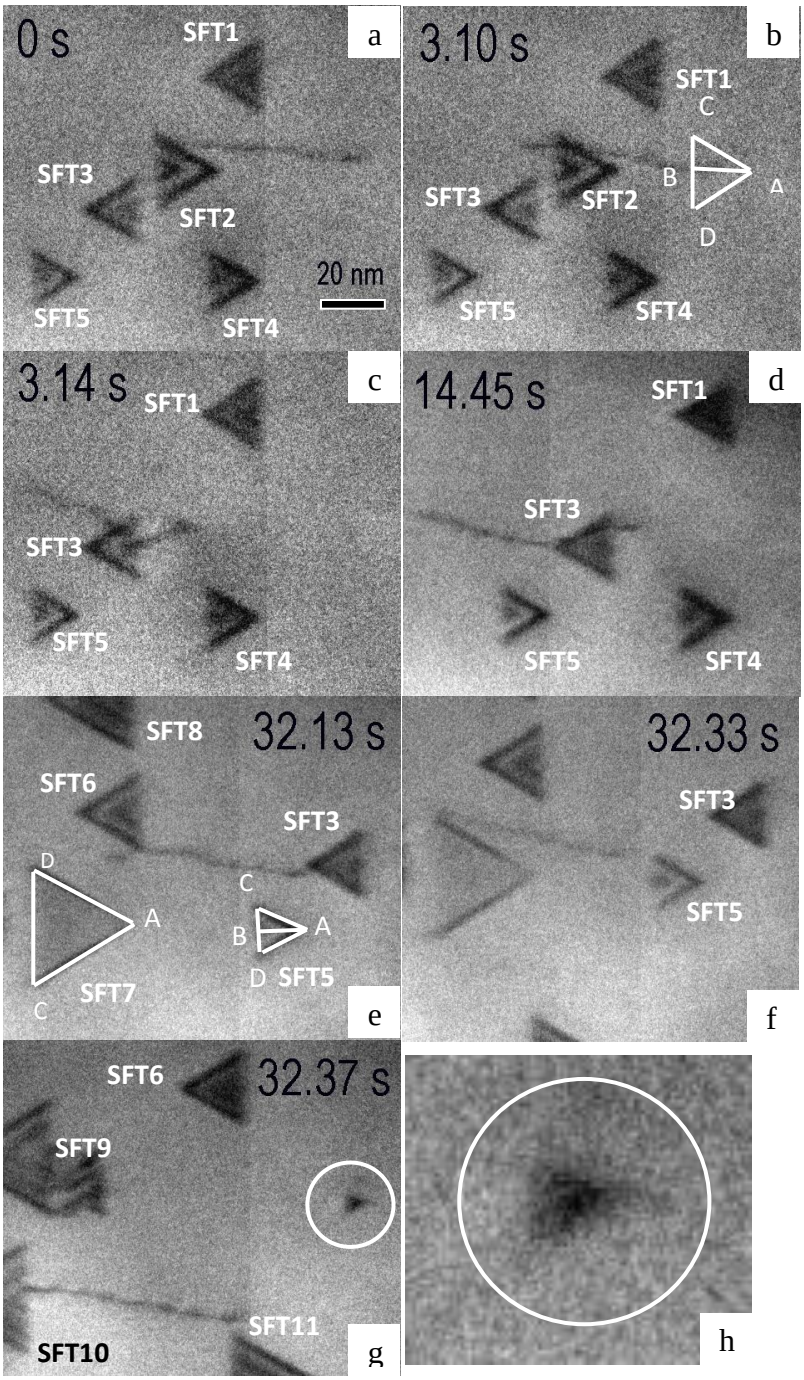

Figure 10. Bright-field electron micrographs of the interaction between three perfect stacking-fault tetrahedra and the same dislocation at 623 K. After the interaction between SFT5 and the moving dislocation, a small stacking-fault tetrahedron (~5 nm) is left behind.

stacking-fault tetrahedron. In Figure 10a and 10b the dislocation, which was determined to determined to have a Burgers vector of $(1\bar{1}0)$, BA, and to be moving on the d-plane (ABC), approaches and interacts with tetrahedron designated SFT2. As a consequence of this

interaction, the tetrahedron is annihilated and the dislocation cross-slips to the c-plane. On this plane it approaches SFT 7 and SFT 5. SFT7 is completely annihilated by the interaction whereas SFT 5 is only partially annihilated. The remnant defect, as shown in the higher magnification image, Figure 10h, is a 5 nm stacking-fault tetrahedron.

Molecular dynamics computer simulations have indicated that the base of a perfect stacking-fault tetrahedron can be absorb by both screw and edge dislocations with the apex portion being left intact [31]. Matsukawa *et al.* [32-34] provided supporting experimental results for this interaction at room temperature. However, in our observations the small remnant defect does not correspond with the apex of the original tetrahedron suggesting perhaps there is a subtle difference with increasing temperature.

To aid the interpretation of the interactions of dislocations with stacking-fault tetrahedra the experimental results were compared and contrasted with the results obtained from molecular dynamic computer simulations. At a high level, the simulations and experiments show striking similarities despite the differences in the boundary conditions of the two cases. Both approaches show the interaction and the outcome (formation of a new defect type or shearing of the tetrahedron) are dependent on the character (edge vs. screw) of the dislocation, the size and degree of perfection (complete or truncated) of the tetrahedron, and on the position (near the apex, center or base) at which the slip plane impacts the tetrahedron. A striking difference in the results is that the simulations do not show operation of the classical Kimura-Maddin annihilation process whereas it occurs readily and frequently in the electron transparent foils [35].

Dislocation Interactions with Vacancy Type Dislocation Loops

For the investigation of the interaction of line dislocations with vacancy loops, a section of an Al-0.11Zr billet was sectioned and annealed at 623 K for 15.5 hrs. and oil quenched. The annealed material was then sectioned to a thickness of 200 μm by electric-discharge machining and straining bars of width and length of 3 mm x 10 mm produced. The samples were ground to a thickness of approximately 120 μm with 600 grit SiC paper. The center of the tensile specimen was made electron transparent through twin jet-electropolishing using a solution of 5% perchloric acid in methanol cooled to 248 K.

We have also investigated the interaction of lattice dislocations with dislocations loops. The loops resulted form the thermal treatment schedule of the Al-Zr alloy. Also present in the samples were thin Zr plate-like precipitates. An example of the initial microstructure is shown in Figure 11. The nature of the larger loops, ones showing double-arc lobe contrast, was

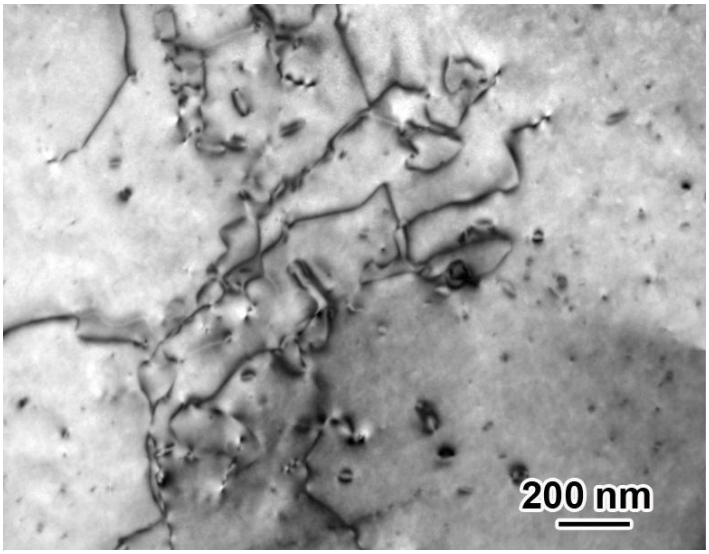

Figure 11. Initial microstructure showing the loops and dislocations in the Al-Zr alloy.

determine to be vacancy by using the "inside-outside" diffraction contrast technique [36]. The nature of the smaller loops, the ones exhibiting black-white lobe contrast was not determined but is inferred to be the same as the larger loops. Several interactions of lattice dislocations with the dislocation loops were observed and some are illustrated in Figures 12, 14 and 16.

An example of loop motion and annihilation during room temperature straining is shown in the series of captured video-frame images presented in Figure 12. When the line dislocation is within 70 nm of the loop, the loop "feels" the presence of the line dislocation and moves. The matrix dislocation essentially pushes the loop ahead of it until the loop motion is hindered by other dislocations. The mobile lattice dislocation then captures and annihilates the loop. The total distance moved by the loop is nominally 125 nm, as can be seen in the image presented in Figure 12f, which is a composite image created by superimposing a negative image (black objects become white) of Figure 12d on a positive image of Figure 12a. The resultant image shows the distance the loop is pushed before being captured and annihilated by the line

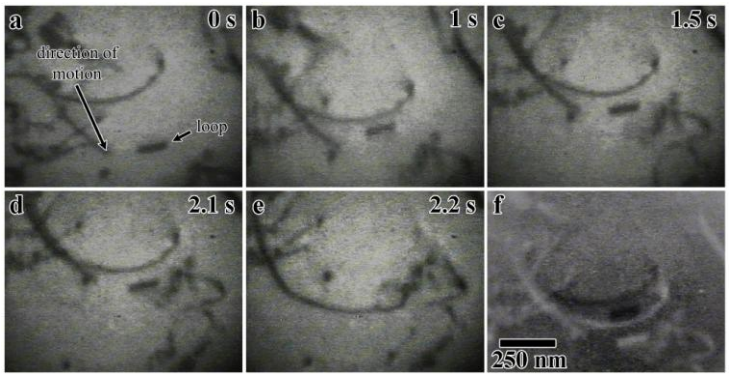

Figure 12. Dislocation loop being repelled by an approaching line dislocation in Al-0.11Zr during in-situ straining experiment at room temperature.

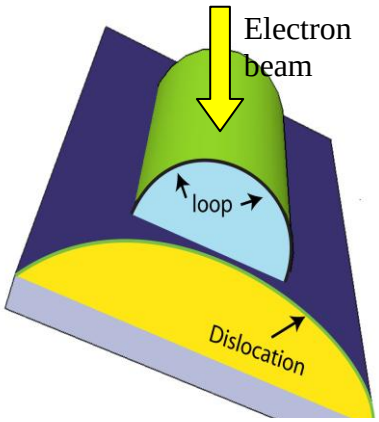

Figure 13. Schematic of the interactions from the perspective of the line dislocation.

dislocation. A schematic showing the interaction as viewed from behind the dislocation is shown in Figure 13; the half cylinder represents the glide surface of the dislocation loop that exists above the slip plane of the line dislocation.

The series of video-frame images shown in Figure 14 presents a common interaction in which a loop appears to rotate as a consequence of the interaction with a line dislocation. This apparent rotation is easily visualized by considering the major axis of the loop, which is indicated by the white lines in Figures 14a and 14f. In this case, the major axis changes by some 17 degrees following the interaction with the dislocation. To understand this apparent effect, it is important to remember that an electron micrograph is a two-dimensional projection on the electron exit surface of the three-dimensional internal structure. Assuming, for discussion, that the loop is circular, a rotation could be attributed to the loop changing habit plane, to a segment of it cross-slipping out of the glide cylinder, or to motion of a segment of the loop along the glide cylinder. In FCC metals unlike in BCC ones, the loops form on the {111}-planes and so the degree of rotation observed cannot be attributed to the loop forming on one plane and rotating to another. Cross-slip, through the motion of the screw component is possible but the angles are not consistent with this operation. The final possibility is that a segment of the loop moves along the glide cylinder with the opposing segment pinned. Such an operation would result in an apparent rotation of the loop image as well as an increase in size. The schematic in Figure 15a

shows two possible movements along the glide cylinder that would result in a change in the projected direction of the major axis as well as an apparent change in the loop diameter. In comparing Figure 15b and 15c, which are just higher magnifications of Figures 14a and 14f, the

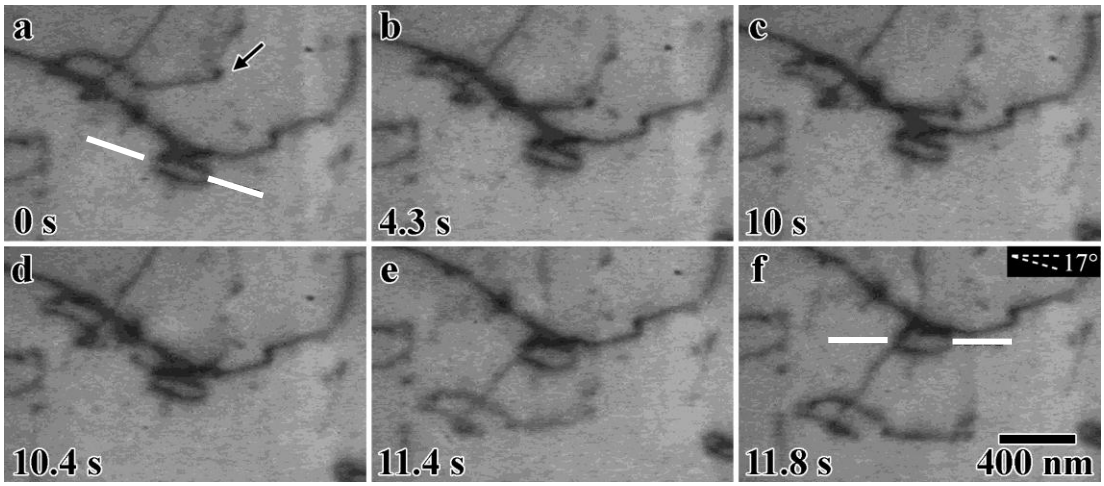

Figure 14. Loop "rotation" resulting from the interaction with the dislocation loop.

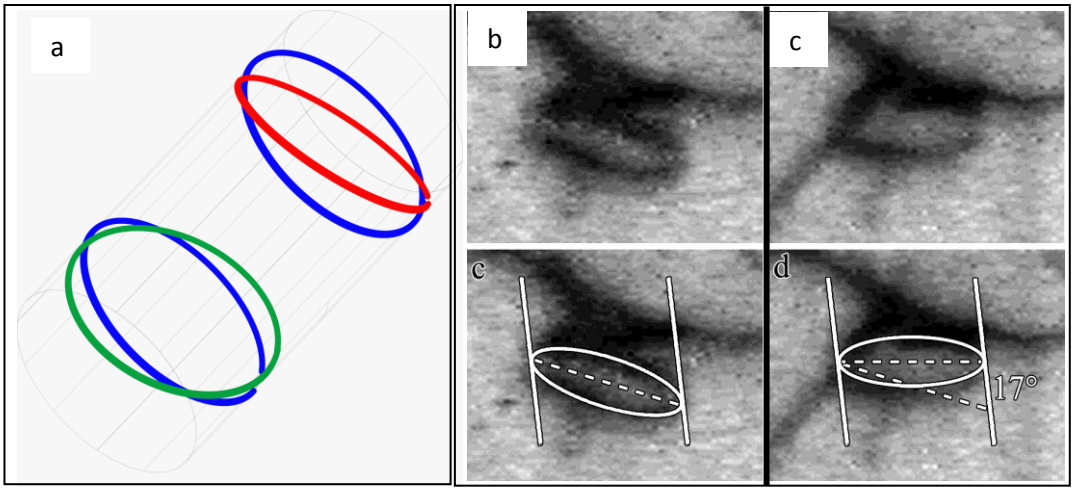

Figure 15. Schematic illustrating apparent change in size and axes with motion of different segments of the loop.

rotation of the major and minor axes of the ellipse and the change in size are obvious. From these interactions we surmise that this image rotation is attributable to one side of the line dislocation moving along the glide cylinder while the other side remains fixed. The pinning of one side and not the other is most likely a consequence of the local stress or chemical environment.

Another type of non-destructive interaction involves loop drag by the glissile dislocation. An example of such an interaction is shown in Figure 16, in which a series of micrographs showing a complex dislocation interaction sequence with a loop are presented. The dynamics of the interaction are shown in the schematic with the dislocations involved in the sequence illustrated in different colors; the dotted lines indicate the previous position and the solid lines

the new one. The outcome of this interaction is that the dislocation loop has been dragged by the line dislocation to a new location and is then incorporated in another line dislocation.

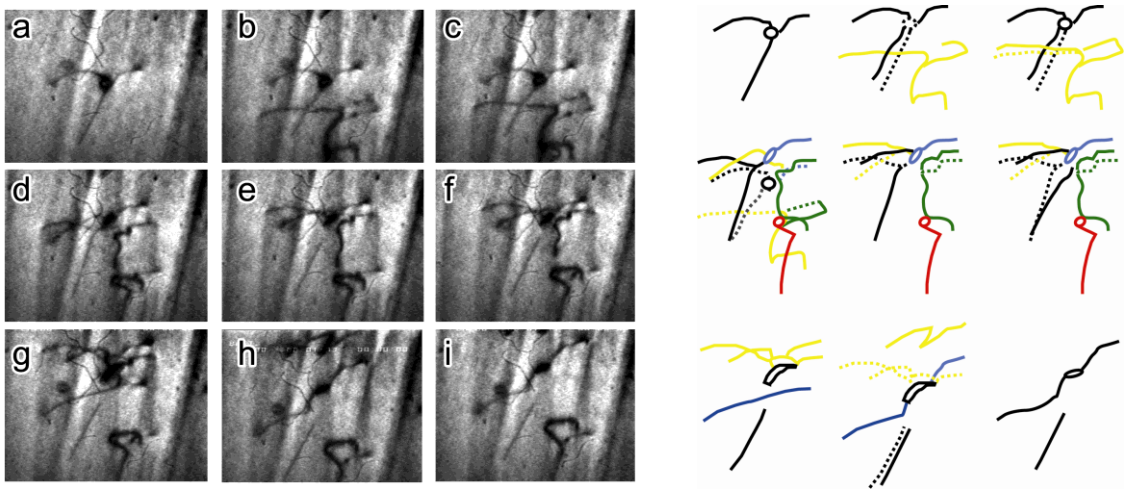

Figure 16. Complex dislocation loop interaction that results in the dragging of the loop by the dislocation and its partial accommodation into one of the reacting dislocations. The dotted lines indicated the previous location and the solid lines the new location.

We have shown that a dislocation loop "feels" the presence of a line dislocation from several hundred nanometers distance and it moves in response to the presence of the line dislocation. To determine if this is reasonable, the long-range elastic interaction between a dislocation and a loop was estimated using linear elastic theory.[37-39] In the following, we adopt the approach of Makin[38] and consider the specific rather than general case as illustrated in the diagram presented in Figure 17. The line dislocation lies along x_3 and is of mixed character with the screw component of the Burgers vector along x_3 and the edge component parallel to x_1. The loops are shown on the faces of a cube, with the loop normal and Burgers vector indicated for normal b_i^{lp}, n_i^{lp} and glide $b_i^{lg\,i}, n_i^{lp1}$ loop configurations.

The force exerted by a line dislocation on a dislocation loop can be calculated from $F = -\left(\frac{dE}{dx_i}\right)$. In this expression, E is the work that must be done to create the loop in the stress field of the dislocation. Assuming that the stress components of the line dislocation are constant over the loop (acceptable if the distance from the loop to the dislocation is greater than the loop radius), the elastic energy is given by $E = \sum_{ij} b_i^l n_j^l A \sigma_{ij}$ where

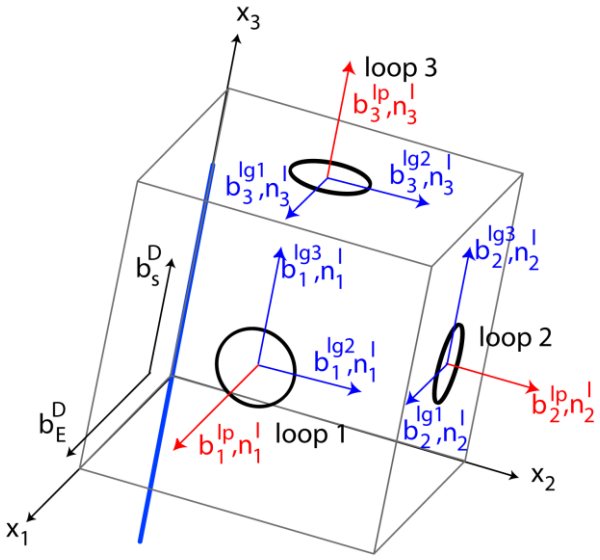

Figure 17. Definition of the dislocation and dislocation loop parameters.

b_i^l is the component of the loop Burgers vector in the *i-direction*, $n_j^l A$ is the projected loop area in a plane perpendicular to the *j-direction*, and σ_{ij} is the stress-field components of the dislocation. For a dislocation interacting with loops having a Burgers vector parallel to the loop normal, it can be verified that the screw component exerts no force on any of the three dislocation loop configurations shown in Figure 17 with $b_i^{lp} \| n_i^{lp}$. Therefore, it is necessary to consider the effect of the edge dislocation component only. For the case of the edge dislocation on a prismatic loop with a Burgers vector and habit plane normal in the *x_1-direction*, the interaction energy is then given by

$$E = An_1^l b_1^l \sigma_{11} \tag{0.1}$$

and the force by

$$F_{x1} = -\left(\frac{dE_1}{dx_1}\right). \tag{0.2}$$

The dislocation stress field component is given by

$$\sigma_{11} = -\frac{Gb_E^D\left(3x_1^2 + x_2^2\right)}{2\pi\left(1-\upsilon\right)\left(x_1^2 + x_2^2\right)^2} \tag{0.3}$$

where G is the shear modulus and υ is Poisson's ratio. The force is then given by

$$F_{x1} = -\left(\frac{dE_1}{dx_1}\right) = An_1^l b_1^l \frac{Gb_E^D 2\left(x_1^2 \diagup x_2^2\right)\left(1-\frac{3x_1^2}{x_2^2}\right)}{2\pi\left(1-\upsilon\right)x_2^2\left(\frac{x_1^2}{x_2^2}+1\right)^3}. \tag{0.4}$$

Setting

$$\varphi = \frac{2\left(x_1^2 \diagup x_2^2\right)\left(1-\frac{3x_1^2}{x_2^2}\right)}{\left(\frac{x_1^2}{x_2^2}+1\right)^3} \tag{0.5}$$

gives

$$F_{x1} = An_1^l b_1^l \frac{Gb_E^D \varphi}{2\pi\left(1-\upsilon\right)x_2^2}. \tag{0.6}$$

The function φ is plotted against $\frac{x_1}{x_2}$ in Figure 18. This shows that for a positive Burgers vector and for a position $\frac{x_1}{x_2} > 0.6$, the function φ is negative which gives a negative force. That is, the force on the loop acts in the negative direction, toward the line dislocation and the loop will be

attracted toward the line dislocation. For $\frac{x_1}{x_2}$ < -0.6, φ and the force are positive, which means that the force on the loop is in the positive direction and again is towards the line dislocation. That is in this range, the force on the loop is attractive and it will move toward the line dislocation. Changing the sign of the Burgers vector of either the loop or the line dislocation will change the direction of the force on the loop, causing the interaction to always be repulsive in these limits.

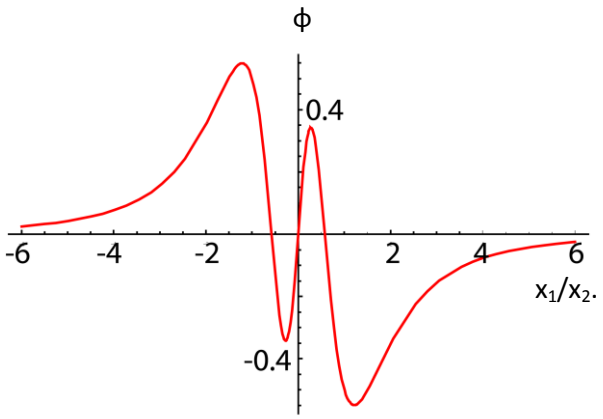

Figure 18. Dependence of φ on x_1/x_2.

The maximum force occurs at a distance $\frac{x_1}{x_2}$ = 1.15, giving

$$F_{\max.} = \frac{An_1^l b_1^l G b_E^D}{2\pi(1-\upsilon)}\left(\frac{0.55}{x_2^2}\right). \tag{0.7}$$

Assuming the magnitude of the critical shear stress, τ_{CSS}, for loop motion is known, the distance from the dislocation to the loop at which this maximum force occurs can be determined from

$$F_{\max.} = \frac{An_1^l b_1^l G b_E^D}{2\pi(1-\upsilon)}\left(\frac{0.55}{x_2^2}\right) \le \tau_{CSS} 2\pi r b. \tag{0.8}$$

From this expression it can be seen that the distance at which the loop first experiences the effect of the dislocation is inversely proportional to the square root of τ_{CSS}, meaning that the distance will increase for smaller values of τ_{CSS}.

The other situation to consider is the force exerted by a line dislocation on a shear loop. For shear loops both edge and screw dislocations can have an impact, although both dislocation types do not interact on all shear loops. For example, considering shear loop 1 with a Burgers vector of $b^{lg2,n1}$ in Figure 17, the shear stress from the screw dislocation that acts on this loop is

$$\sigma_{23} = \frac{Gb_S}{2\pi}\frac{x_1}{x_1^2 + x_2^2}. \tag{0.9}$$

The resultant interaction energy is given by

$$\frac{AnGb^S b^{lg2,n1}}{2\pi}\left[\frac{x_1}{\left(x_1^2 + x_2^2\right)}\right]. \tag{0.10}$$

The forces in the x_1- and x_2-direction are found by differentiating with respect to x_2 and x_1, respectively. This yields for the force in the x_1 direction

$$-\frac{AnGb^S b^{\lg 2,n1}}{2\pi}\left[\frac{2x_1 x_2}{\left(x_1^2+x_2^2\right)^2}\right]=-\frac{AnGb^S b^{\lg 2,n1}}{2\pi \quad x_2^2}2\left[\frac{x_1/x_2}{\left(1+x_1^2/x_2^2\right)^2}\right]=-\frac{AnGb^S b^{\lg 2,n1}}{2\pi \quad x_2^2}\varphi, \quad (0.11)$$

$$where \quad \varphi=2\left[\frac{x_1/x_2}{\left(1+x_1^2/x_2^2\right)^2}\right] \quad (0.12)$$

and for the force in the x_2 direction

$$\frac{AnGb^S b^{\lg 2,n1}}{2\pi}\left[\frac{x_1^2-x_2^2}{\left(x_1^2+x_2^2\right)^2}\right]=\frac{AnGb^S b^{\lg 2,n1}}{2\pi \quad x_1^2}\left[\frac{1-x_2^2/x_1^2}{\left(1+x_2^2/x_1^2\right)^2}\right]=\frac{AnGb^S b^{\lg 2,n1}}{2\pi \quad x_1^2}\varphi, \quad (0.13)$$

$$where \quad \varphi=\left[\frac{1-x_2^2/x_1^2}{\left(1+x_2^2/x_1^2\right)^2}\right] \quad (0.14)$$

The functions φ are plotted in Figure 19a; the equivalent functions for the influence of an edge dislocations acting on the same loop are shown in Figure 19b. The force F_{x_2} due to the screw dislocation is negative for x_2^2/x_1^2 >1 so the loop will be attracted toward the loop but will stop at x_2/x_1 =1. For x_2/x_1 < -1, φ is again negative so the force acting on the loop will be negative. Thus the force acts in the negative direction and repels the loop. In the F_{x_1} direction, φ is positive for all positive values of x_2/x_1 so the force will act in the negative direction. That is this component will tend to attract the dislocation toward the loop. φ is negative for all negative

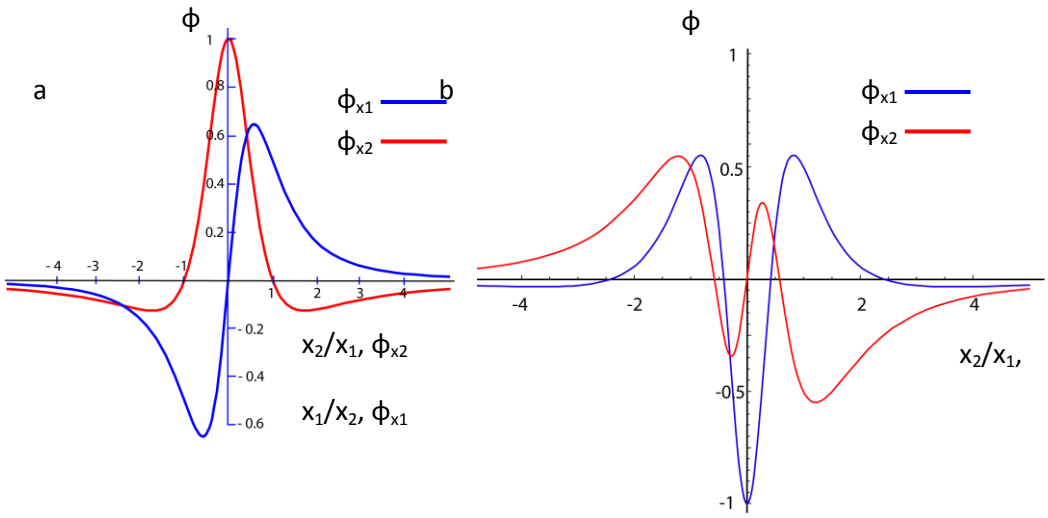

Figure 19 a) the effective force on the loop due to screw component of the line dislocation and b) the effective force on the loop due to edge component of the line dislocation.

values of x_2/x_1 so the force acts in the positive direction and the loop is attracted to the dislocation. The maximum in the force occurs at a value x_2/x_1 = 0.54, and is given by $\frac{AnGb^S b^{\lg 2,n1}}{2\pi \quad x_2^2} 0.65$. This expression shows again that the distance at which the loop experiences the line dislocation is inversely proportional to the square root of the critical shear stress.

Dislocation interactions with voids and bubbles.

For the investigation of the interaction of dislocations with bubbles, nickel, 99.999% purity and 90 µm-thick, foils were implanted at temperatures from 293 K to 773 K with He^+ ions with energies ranging from 140 to 300 keV. Specific details on the irradiations, which were performed at Los Alamos National Laboratory, are given in Table 1. Discs, 3 mm-diameter were punched out of the implanted foils, wrapped in tantalum foil and annealed in vacuum at 1023 K for times between 1 and 2 hours. To access the implanted damage region, the discs were electropolished from the unirradiated side to a thickness of approximately 45 µm, the protective coating on the irradiated side removed and the disc electropolished from both sides to penetration. For electropolishing, an electrolyte of 10% perchloric acid in methanol at 243 K and a current density of 0.15 Acm^{-2} were used. In situ TEM straining specimens of dimensions 10 mm x 3 mm were also cut from the implanted foils and subjected to the same preparation process.

Small helium bubbles show weak contrast in a focused dynamical and kinematical bright-field imaging condition. They are rendered visible in under- and over-focused conditions appearing with a bright surrounding ring in under-focused images and with a dark interior

Table 1. Implantation conditions.				
Samples	Ion Dose (at/cm^2)	Ion Energy (keV)	Temperature (K)	Implantation depth (nm)
Ni-a	$1x10^{13}$	300	293	660
Ni-b	$1x10^{14}$	300	293	660
Ni-c	$1x10^{15}$	160	293	418
Ni-d	$1x10^{16}$	160	293	418
Ni-1	$2x10^{14}$	160	573	418
Ni-2	$2x10^{14}$	160	673	418
Ni-3	$2x10^{14}$	160	773	418

ring in over-focused conditions, Figure 20. Larger bubbles or voids are visible under in-focus images as shown in Figure 21 for bubbles produced by annealing at 1023 K. The shape of the bubbles formed changes with increasing size. This change in projected image is consistent with the work of Chen [40]which showed that there are five possible shapes of voids produced in irradiated Nickel; see Table 2. The octahedral void with appreciable truncation on the {100} surfaces is the type most often observed.

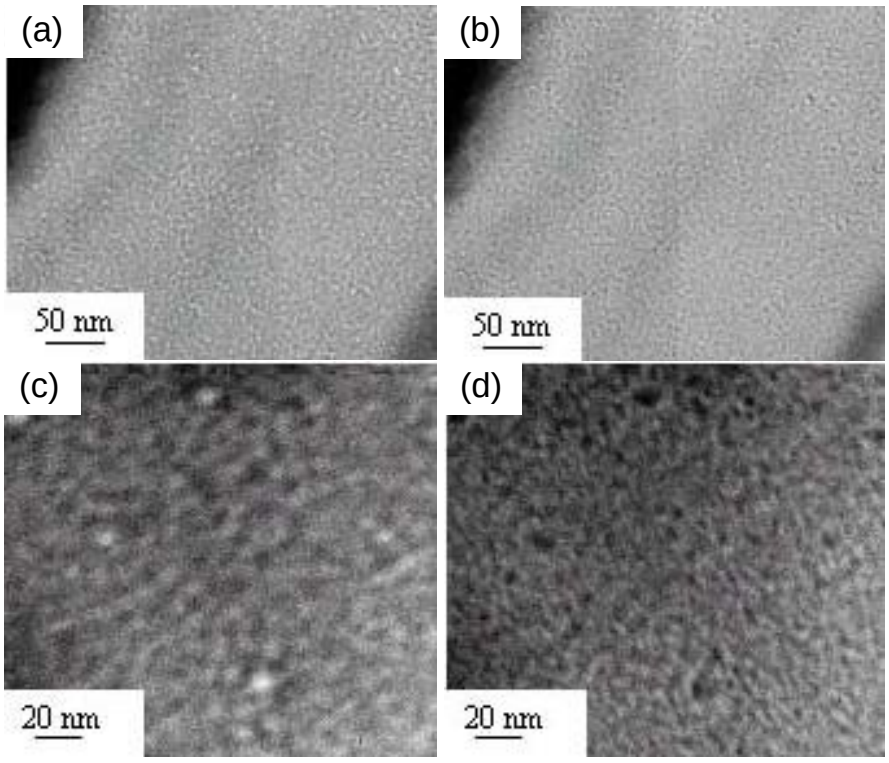

Figure 20. TEM defocus contrast images of He bubbles in irradiated samples. (a)-(b) Ni-1 sample in under-focused and over-focused BF images, respectively; and (c)-(d) Ni-a sample in under-focused and over-focused BF images, respectively.

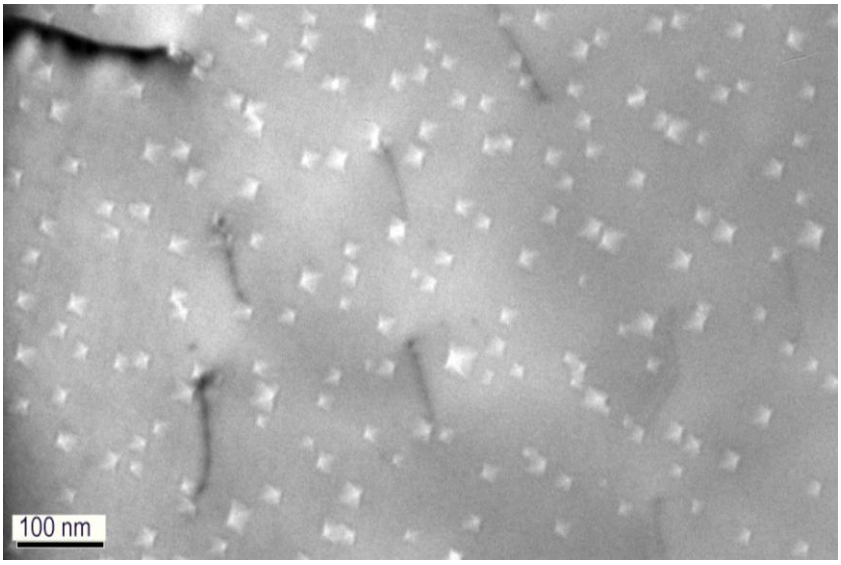

Figure 21: TEM under-focused BF image of He bubbles in sample designated Ni-1 showing the shapes of cavities after annealing at 750°C for 2 hours.

Table 2. TEM projections predicted for voids of different shapes: **A** Octahedral, **B** Octahedral with {100} truncation, **C** Cubo-Octahedral, **D** Cubic with {111} truncation and **E** Cubic. The diffraction contrasts are given for the (100) and (110) projections [2].

crystal direction in which the incident beam lies		A	B	C	D	E
1	[100]	$01\bar{1}$ 011	$01\bar{1}$ 011	010 001	010 001	010 001
2	[110]	$01\bar{1}$ $10\bar{1}$	$01\bar{1}$ $1\bar{1}0$ $10\bar{1}$	$1\bar{1}0$ 011 $0\bar{1}1$	$1\bar{1}0$ 011 001	$1\bar{1}0$ 001
3	[111]	110 011 101	$10\bar{1}$ 110 $01\bar{1}$ 011 101 110	$\bar{1}01$ $0\bar{1}1$ $\bar{1}10$	001 $0\bar{1}1$ $10\bar{1}$ $0\bar{1}0$ $1\bar{1}0$ 100	001 $0\bar{1}0$ 100

A quantitative analysis of the distribution and size of the bubbles was performed for the specimen irradiated at high temperature and subsequently annealed at 1023 K for 2 hours; the results of this analysis are presented in Table 3. The size of the bubbles was determined from under-focus images as in this condition the contrast is directly related to the defect width [41]. For the different specimens, the same micrograph area was considered in each of the samples.

Table 3. Areal density of He bubbles in different size ranges and the average bubble diameter.

sample	Area examined ($x10^{-8}$ cm^2)	Implantation temperature (K)	Number of Helium bubbles within area having a diameter in the specified range.			Average diameter of the He bubbles. (nm)
			<15 nm	15-35 nm	> 35 nm	
Ni-1	9.5	573	57	100	3	19.9 ± 8.2
Ni-1	9.5	573	53	106	1	20.3 ± 7.7
			<40 nm	40-60 nm	> 60 nm	
Ni-3	0.42	773	3	5	8	63.5 ± 24.5
Ni-3	0.42	773	0	5	4	60.2 ± 9.5
Ni-3	0.42	773	5	6	6	50.1 ± 19.6

The interaction between dislocations and bubbles is difficult to unravel. For situations in which the spacing between bubbles is less than the dislocation line length the interaction is complex with dislocation segments forming on the bubbles. These segments disrupt the interaction with other dislocations and rearrangements occur locally before dislocations break free. An example of this behavior is shown in the time series of images presented in Figure 22. Here the dislocation positions are transferred to later images to assist in the comparison of the reactions. Dislocations 1 and 2 are already attached to the bubbles and dislocation 3 is seen

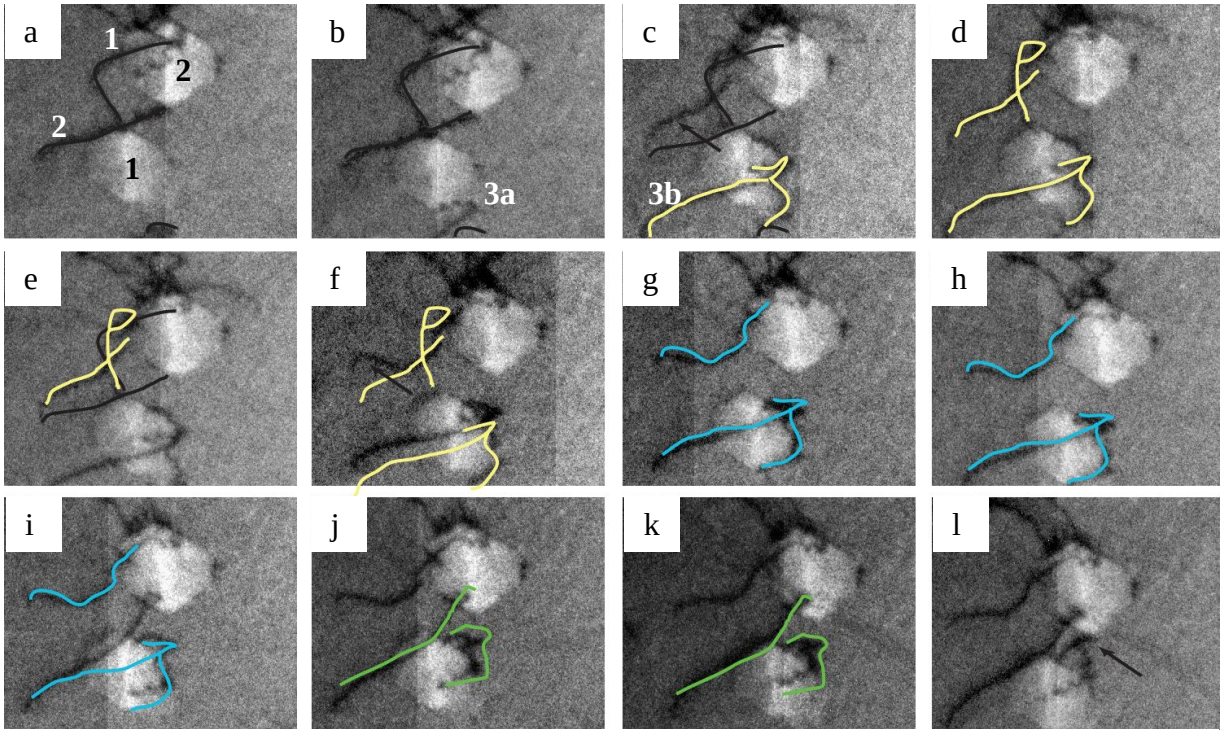

Figure 22. Interaction dislocations with large He bubbles. Bright-field electron micrographs of Helium bubbles pinned by dislocations in Ni-c sample that was annealed at 1023 K for 2 hours after irradiation. The bubbles, which are clearly pinning the dislocations, are 80-90 nm

approaching one of the bubbles; although only a short segment of dislocation 3 is seen in Figure 22a, it actually has a complex shape consistent with it having cross-slipped and is now existing on two slip planes. One segment of dislocation 3 interacts with the bubble in Figure 22b and remains locked in contact with it. The other segment, dislocation 3b, which is able to move independently and passes the pinned segment as evidenced by the new dislocation that appears in Figure 22c. The dislocation configurations change by small amounts only during this period and the first dislocation to break free is dislocation 1, Figure 22g. Dislocation 3a remains attached to the bubble and it appears to expand to form a half loop between the two bubbles. Segment 3b continues to bypass the bubble but it does not break free. The complex dislocation arrangement attached to bubble 2 undergoes some rearrangement during this time but no dislocations are released. The complexity of the dislocation interactions with the bubbles continues with increasing strain as can be seen in the image presented in Figure 23. Some of the original dislocations remain attached and a few additional ones have been added.

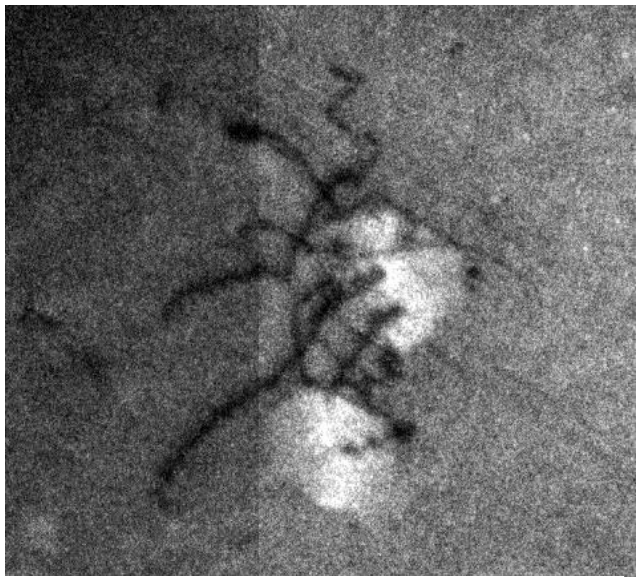

Figure 23. Dislocation interactions with two closely spaced bubbles.

As observed in the reported interactions between dislocations and stacking-fault tetrahedra and the loops and reported elsewhere for interactions with particles [42, 43], the interaction with bubbles is dependent on the impact location. That is the distance from the center of bubble to the glide is an important parameter in determining the obstacle strength and the sequence of interaction events. Hatano and Matsui [44]incorporated this parameter in their molecular dynamic simulations and they found that a dislocation can be strongly pinned if the distance of the slip plane from the bubble center, d, is in the range $-0.1r \leq d \leq 0$, where r is the radius of the bubble. For $d > 0$, the pinning strength becomes considerably weaker, suggesting that the hydrostatic pressure is dominant over the shear stress. In the current study it was noted that the approaching dislocation, provided it has a high screw character, can cross-slip at some distance from the bubble so that the nature of the interaction is changed, presumably cross-slip is activated to minimize the interaction energy with the obstacle. This was different from interactions with stacking-fault tetrahedra in which the slip plane of screw dislocations was often the conjugate slip plane following the interaction with the tetrahedra.

Summary

These observations reveal the complexity of the interactions involving dislocations and different obstacles. The pushing and dragging of the loops by the mobile dislocations provide a means to further reduce the debris produced in channels observed in deformed irradiated material. These interactions and processes provide the missing link for explaining why the channels are free of debris. The interactions with the stacking-fault tetrahedra at elevated temperature show reactions

similar to those observed at room temperature, with no significant change in mechanism with the increased ability for dislocation climb or pipe diffusion along the dislocation. The interactions with voids and bubbles illustrate they are strong pinning centers, although the details of the interaction and the bypass processes remain to be determined. The present study is for a limited set of materials so it is inappropriate to make claims of general bypass processes and further efforts in different materials are needed before generalities that can form the foundation of constitutive relationships can be drawn.

References.

[1] Roberto J, Rubia T. Diaz de la. Basic Research Needs For Advanced Nuclear Energy Systems. http://www.science.doe.gov/bes/reports/files/ANES_rpt.pdf 2006.

[2] Bailat C, Groschel F, Victoria M. Deformation modes of proton and neutron irradiated stainless steels. Journal of Nuclear Materials 2000;276:283.

[3] Bailat C, Almazouzi A, Baluc N, Schaublin R, Groschel F, Victoria M. The effects of irradiation and testing temperature on tensile behaviour of stainless steels. Journal of Nuclear Materials 2000;283-287:446.

[4] Dai Y. Mechanical Properties and Microstructures of Copper Gold and Palladium Single Crystals Irradiated with 600 MeV Protons. Departement of Physics. Lausanne: Ecole Polytechnique Federale De Lausanne (EPF), 1995. p.129.

[5] Diaz de la Rubia T, Zbib HM, Khraishi TA, Wirth BD, Victoria M, Caturla MJ. Multiscale modelling of plastic flow localization in irradiated materials. Nature 2000;406:871.

[6] Eyre BL. Small clusters and their influence on mechanical properties in irradiated metals. International Metallurgical Reviews 1974;19:240.

[7] Linga Murty K. Role and significance of source hardening in radiation embrittlement of iron and ferritic steels. Journal of Nuclear Materials 1999;270:1.

[8] Lucas GE. The evolution of mechanical property change in irradiated austenitic stainless steels. Journal of Nuclear Materials 1993;206:287.

[9] Singh BN, Edwards DJ, Toft P. Effect of neutron irradiation and post-irradiation annealing on microstructure and mechanical properties of OFHC-copper. Journal of Nuclear Materials 2001;299:205.

[10] Victoria M, Baluc N, Bailat C, Dai Y, Luppo MI, Schaublin R, Singh BN. Microstructure and associated tensile properties of irradiated FCC and BCC metals. Journal of Nuclear Materials 2000;276:114.

[11] Wirth BD, Odette GR, Marian J, Ventelon L, Young-Vandersall JA, Zepeda-Ruiz LA. Multiscale modeling of radiation damage in Fe-based alloys in the fusion environment. vol. 329-333. Kyoto, Japan: Elsevier, Amsterdam, Netherlands, 2004. p.103.

[12] Robach JS, Robertson IM, Wirth BD, Arsenlis A. In-situ transmission electron microscopy observations and molecular dynamics simulations of dislocation-defect interactions in ion-irradiated copper. Philosophical Magazine A 2003;83:955.

[13] Robertson IM, Beaudoin A, Al-Fadhalah K, Chun-Ming L, Robach J, Wirth BD, Arsenlis A, Ahn D, Sofronis P. Dislocation-obstacle interactions: Dynamic experiments to continuum modeling. Materials Science and Engineering A 2005;400-401:245.

[14] Arsenlis A, Wirth BD, Rhee M. Dislocation density-based constitutive model for the mechanical behaviour of irradiated Cu. Philosophical Magazine 2004;84:3617.

[15] Aidi B, Viltange M, Dimitrov O. Influence of the local order on the mechanical properties of austenitic Fe-Cr-Ni alloys. Journal of Nuclear Materials 1990;175:1.
[16] Himbeault DD, Chow CK, Puls MP. Deformation behavior of irradiated Zr-2.5Nb pressure tube material. Metallurgical & Materials Transactions A Physical Metallurgy & Materials Science 1994;25A:135.
[17] Muller GV, Gavillet D, Victoria M, Martin JL. Post irradiation tensile properties of Mo and Mo alloys irradiated with 600 MeV protons. Journal of Nuclear Materials 1994;212-215:1283.
[18] Shinohara K, Yasuda M, Yasuda K, Kutsuwada M. Effects of 100 keV He-ion irradiation on early stage of plastic deformation of copper polycrystals at 77 K. Journal of Nuclear Materials 1991;182:145.
[19] Singh BN, Horsewell A, Toft P, Edwards DJ. Temperature and dose dependencies of microstructure and hardness of neutron irradiated OFHC copper. Journal of Nuclear Materials 1995;224:131.
[20] Clark BG, Robertson IM, Dougherty LM, Ahn DC, Sofronis P. High-temperature dislocation-precipitate interactions in Al alloys: an in situ transmission electron microscopy deformation study. Journal of Materials Research 2005;20:1792.
[21] Baluc N, Schaublin R, Bailat C, Paschoud F, Victoria M. Mechanical properties and microstructure of the OPTIMAX series of low activation ferritic-martensitic steels. Journal of Nuclear Materials 2000;283-287:731.
[22] Singh BN, Golubov SI, Trinkaus H, Edwards DJ, Eldrup M. Review: evolution of stacking fault tetrahedra and its role in defect accumulation under cascade damage conditions. Journal of Nuclear Materials 2004;328:77.
[23] Dai Y, Jia X, Chen JC, Sommer WF, Victoria M, Bauer GS. Microstructure of both as-irradiated and deformed 304L stainless steel irradiated with 800 MeV protons. Journal of Nuclear Materials 2001;296:174.
[24] Moya G. Kinetics of vacancy precipitation during the formation of stacking- fault tetrahedra in quenched gold. Acta Metallurgica 1975;23:289.
[25] Kimura H, Maddin R. Quench Hardening in Metals. London: North-Holland, 1971.
[26] Kimura H, Maddin R, Kuhlmann-Wilsdorf D. Quenched-In Vacancies in Noble Metals-II Mechanism of Quench Hardening. Acta Metallurgica 1959;7:154.
[27] Tawara T, Matsukawa Y, Kiritani M. Defect structure of gold introduced by high-speed deformation. Materials Science & Engineering A (Structural Materials: Properties, Microstructure and Processing) 2003;A350:70.
[28] Kiritani M. Dislocation-free plastic deformation under high stress. Materials Science & Engineering A (Structural Materials: Properties, Microstructure and Processing) 2003;A350:1.
[29] Hirth JP, Lothe J. Theory of dislocations. New York: Wiley, 1982.
[30] Kimura H, Maddin R. Effect of Quenched-In Vacancies on the Mechanical Properties of Metals and Alloys. In: Cotterill R, editor. Lattice defects in quenched metals; an international conference held at the Argonne National Laboratory, June 15-17, 1964, sponsored by the United States Atomic Energy Commission. New York: Academic Press, 1965. p.319.
[31] Osetsky YN, Rodney D, Bacon DJ. Atomic-Scale Study of Dislocation-Stacking Fault Tetrahedron Interactions. Philosophical Magazine 2006:2295.

[32] Matsukawa Y, Osetsky YN, Stoller RE, Zinkle SJ. The collapse of stacking-fault tetrahedra by interaction with gliding dislocations. Materials Science & Engineering A (Structural Materials: Properties, Microstructure and Processing) 2005;400-401:366.
[33] Matsukawa Y, Osetsky YN, Stoller RE, Zinkle SJ. Destruction processes of large stacking fault tetrahedra induced by direct interaction with gliding dislocations. Journal of Nuclear Materials 2006;351:285.
[34] Matsukawa Y, Zinkle SJ. Dynamic Observation of the Collapse Process of a Stacking Fault Tetrahedron by Moving Dislocations. Journal of Nuclear Materials. 2004;329-333:919.
[35] Matsukawa Y, Briceno M, Robertson. IM. Combining in situ Transmission Electron Microscopy and Molecular Dynamics Computer Simulations to Reveal the Interaction Mechanisms of Dislocations with Stacking-fault Tetrahedron in Nuclear Materials. Journal of Microscopy Technique;in press.
[36] Jenkins ML, Kirk MA. Characterization of radiation damage by transmission electron microscopy. Bristol ; Philadelphia: Institute of Physics Pub., 2001.
[37] Kroupa F. Interaction between prismatic dislocation loops and straight dislocations -- 1. Philosophical Magazine 1962;7:783.
[38] Makin MJ. The Long-range Forces between Dislocation Loops and Dislocations. Philosophical Magazine 1964;10:695.
[39] Wolfer WG. Image stresses of dislocation loops and lenticular inclusions, and their effects. Philosophical Magazine Letters 2003;83:677.
[40] Chen CW. The Shapes of Irradiation-Produced Voids in Nickel. Physica Status Solidi 1973;16:197.
[41] Edington JW. Practical Electron Microscopy in Materials Science, 1976.
[42] Robertson IM, Wirth BD, Li CM, Clark B, Vandersall JA. Dislocation - Radiation obstacle interactions: Developing improved mechanical property constitutive models. vol. 93. Washington, D.C., United States: American Nuclear Society, La Grange Park, United States, 2005. p.473.
[43] Clark BG, Dougherty LM, Robertson IM, Ahn DC, Sofronis P. High-temperature dislocation-precipitate interactions in Al alloys: An in-situ transmission electron microscopy deformation study. Journal of Materials Research 2005;20:1792.
[44] Hatano T, Kaneko T, Abe Y, Matsui H. Void-induced cross slip of screw dislocations in fcc copper. Physical Review B (Condensed Matter and Materials Physics) 2008;77:064108.